Original article

Meiling Zhang, Hui Wang*, Ting Nie, Jintao Bai, Fei Zhao and Shenghua Ma*

Enhancement of barrier and anti-corrosive performance of zinc-rich epoxy coatings using nano-silica/graphene oxide hybrid

https://doi.org/10.1515/corrrev-2020-0034
Received April 24, 2020; accepted August 22, 2020;
published online October 28, 2020

Abstract: This study reports a facile method to prepare silica-coated graphene oxide nanoflakes (SiO_2–GO). Results of X-ray diffraction analysis, Raman spectroscopy, Fourier transform infrared spectroscopy, scanning electron microscopy, transmission electron microscopy and atomic force microscopy reveal that silica was successfully coated on the GO flakes. The effect of SiO_2–GO nanosheets on the corrosion protection and barrier performance of the epoxy coating was investigated in this work. Results indicate that the mechanical properties of all coatings added with GO and SiO_2–GO were significantly improved. Furthermore, electrochemical impedance and Tafer polarisation curves showed that added 0.5 wt% SiO_2–GO nanoflakes into zinc-rich epoxy coating could greatly improve the anti-corrosion performance of the sample, and the corrosion protection efficiency increased from 67.01 to 99.58%.

***Corresponding authors: Hui Wang**, Key Laboratory of Synthetic and Natural Functional Molecule Chemistry (Ministry of Education), College of Chemistry & Materials Science, Northwest University, Xi'an, 710069, P. R. China; Shaanxi Joint Lab of Graphene (NWU), Xi'an, 710127, P. R. China, E-mail: huiwang@nwu.edu.cn; and **Shenghua Ma**, National Key Laboratory of Photoelectric Technology and Functional Materials (Culture Base), National Photoelectric Technology and Functional Materials & Application of International Science and Technology Cooperation Base, Institute of Photonics & Photon-Technology, Northwest University, Xi'an, 710069, P. R. China; Shaanxi Joint Lab of Graphene (NWU), Xi'an, 710127, P. R. China, E-mail: mashenghua@nwu.edu.cn
Meiling Zhang, Ting Nie and Fei Zhao, Key Laboratory of Synthetic and Natural Functional Molecule Chemistry (Ministry of Education), College of Chemistry & Materials Science, Northwest University, Xi'an, 710069, P. R. China; Shaanxi Joint Lab of Graphene (NWU), Xi'an, 710127, P. R. China
Jintao Bai, National Key Laboratory of Photoelectric Technology and Functional Materials (Culture Base), National Photoelectric Technology and Functional Materials & Application of International Science and Technology Cooperation Base, Institute of Photonics & Photon-Technology, Northwest University, Xi'an, 710069, P. R. China; Shaanxi Joint Lab of Graphene (NWU), Xi'an, 710127, P. R. China

Keywords: barrier properties; corrosion resistance; EIS; epoxy coating; SiO_2–GO.

1 Introduction

Organic coatings play an important role in physical barriers and inhibitors between metal surfaces and corrosive media. They can greatly reduce the corrosion rate of metal surfaces and have been widely applied for anti-corrosion protection (Arman et al. 2013; Jalili et al. 2015; Ramezanzadeh et al. 2015, 2016a,b,c) . However, these organic coatings did not provide universal corrosion protection, with some corrosive substances still able to breach the surface of the coating through different corrosion paths (Maksimovic and Miskovic-Stankovic 1992), resulting in accelerated corrosion of the coating surface and the formation of pores and defects (Alam et al. 2013; Liu et al. 2009), thereby decreasing barrier performance. To remedy this defect, many metals or metal oxides were used as fillers in epoxy coating. Adding metallic nanoparticles such as aluminium, titanium and zinc is a general way for enhancing the barrier and anticorrosive performance of epoxy coatings (Schaefer and Miszczyk 2013; Zhang et al. 2007). Zinc power as an organic coatings filler has excellent corrosion resistance in marine environment (Ito et al. 2011). At present, the most widely used organic coatings are zinc-rich epoxy (Zn-EP) coatings. They can protect metal substrate effectively by sacrificing anode to protect cathode. In traditional zinc-rich coatings, active zinc powder was considered to be an anode constituted with iron matrix to compose a "corrosion battery". Iron was protected as cathode because the corrosion potential of zinc was much lower than iron (Akbarinezhad et al. 2011; Gergely et al. 2011; Ramezanzadeh et al. 2017). However, the conductivity of zinc and iron principally relies on the contact of vast zinc powder in the coatings and zinc formed zinc oxide and others formed some corrosion products during the process of anode protecting cathode, greatly impeding zinc-rich epoxy coatings' development (Chavrier et al. 1988). Although it can provide some barrier effect, the coating is

easy to fail due to reduction of the contact between zinc particles and particles (Kalendova et al. 2015; Stejskal et al. 2006). In order to decrease the high porosity of the coating and dosage of zinc powder, diverse inorganic nanofillers have been infused into the polymer matrices. Recently, various methods have been proposed to enhance the interfacial interaction between fillers and the polymer substrate, particularly chemical modification on the surface of nanoparticles.

Compared to conventional fillers, nano-sized materials have small size and large surface area, which could offer an excellent barrier to corrosive electrolyte diffusion (Shi et al. 2003). Graphene is transparent but not penetrable by visible light. It has outstanding electrical conductivity, physical and mechanical properties and shielding of water molecules and air (Bohm 2014). These characteristics make graphene have broad development prospects for application in metal anti-corrosive coatings. However, although graphene provides a good physical barrier, it has high conductivity which accelerates the rate of electrochemical corrosion of the steel surface by forming a conductive path with zinc power in the Zn-EP coating. If the coating has slight cracks or scratches, this accelerates local electrochemical corrosion, resulting in corrosion of the exposed area and reduced strength and toughness of the metal (Cui et al. 2017). It is this effect that has restricted the application of graphene in metal anti-corrosive coatings.

Graphene oxide (GO), made from graphite oxidation, has a two-dimensional hydrophilic lamellar structure (Kim et al. 2010). GO has numerous epoxy groups, hydroxyl, ketone and carboxyl functional groups, which makes it conducive to functionalisation with organic and inorganic materials through chemical cross-linking (Liu et al. 2011). Additionally, GO is amphiphilic with a largely hydrophobic basal plane and hydrophilic edges, which could assist its dispersion in epoxy matrices and combined with epoxy resin networks by covalent bonding (Dreyer et al. 2010; Yu et al. 2015). In recent years, modified nano-sized materials in polymer coatings feature highly protective properties, attracting tremendous attention in materials science. Silane coupling agents have frequently been employed to embellish GO because of their hybrid organic–inorganic structure, allowing them to bind with both organic and inorganic materials (Layek and Nandi 2013; Wang et al. 2013; Yang et al. 2013). Jiang et al. (2015a,b) studied the anti-corrosion performance of EP coating strengthened with active amino silane precursors on Q235 steel. Data analysis indicates that the introduction of silane coupling agents promoted interfacial adhesion bonds and reduced the spalling degree of the coating. Ramezanzadeh et al. (2016a,b,c) investigated that functionalized graphene oxide nanosheet could increase the anti-corrosion performance of epoxy coatings and reduce the cathodic stripping of steel matrix.

From the other point of view, different metal oxides nanofillers such as silica (SiO_2), titania (TiO_2), alumina (Al_2O_3), zinc oxide (ZnO), zirconium oxide (ZrO_2) and iron oxides (Fe_2O_3/Fe_3O_4) also can provide the higher corrosion resistance. These inorganic nanofillers with surface functionalities can increase the coating cross-linking density and enhance its barrier performance (Eduok et al. 2017; Najjar et al. 2018; Shi et al. 2017). They can provide additional advantages for polymer coatings; for example, TiO_2 as an inorganic nanofiller improves the chemical and corrosion stability, it also has good electrical properties, photocatalytic activity and ability to absorb UV light (Mahulikar et al. 2011). Al_2O_3 is widely used to enhance the abrasion resistance of polymer coatings because it is a hard material (Dhoke et al. 2013). Nano ZnO is one of the metal oxide with unique properties including high hardness and low refractive index, high hydrophobicity and barrier performance (Ammar et al. 2016). ZrO_2 with properties such as high strength, fracture toughness, wear resistance, hardness and good chemical resistance is widely used as an anti-corrosive material in polymer coatings (Mirabedini et al. 2012). Like other nanomaterials, nano-silica has a small size and a large surface area, so it has extremely strong ultraviolet absorption. Adding it to the coating as a filler will form an isolated layer on the coating surface, thus achieving the purpose of anti-UV ageing and thermal ageing. In addition, the isolated layer can effectively prevent alien species from invading and avoid the corrosion of the steel substrate. Shi et al. (2009) found that SiO_2 nanoparticles could markedly improve the coating substrate by changing its microstructure, subsequently enhancing both its antiseptic properties and Young's modulus. Therefore, it was decided to investigate a hybrid SiO_2–GO nanofiller, to prepare a nanohybrid material with a unique three-dimensional network structure, to increase the interfacial adhesion and antiseptic performance of Zn-EP coating.

The zinc powder filler in the Zn-EP coating can effectively fill the loose void on the surface of the coating, but there are still obvious gaps between the particles and the particles, so we need to find a material with lamellar structure to fill the gap. Therefore, in this research, SiO_2–GO nanosheet was prepared using TEOS hydrolysis. The prepared SiO_2–GO nanosheet provided a compact oxide film on the Zn-EP coating to remedy the defect of loose Zn-EP coating surface. The schematic illustration of the synthesis of SiO_2–GO nanosheet is shown in Figure 1. The SiO_2–GO was characterised by X-ray diffraction (XRD) analysis, Fourier transform infrared spectroscopy (FT-IR),

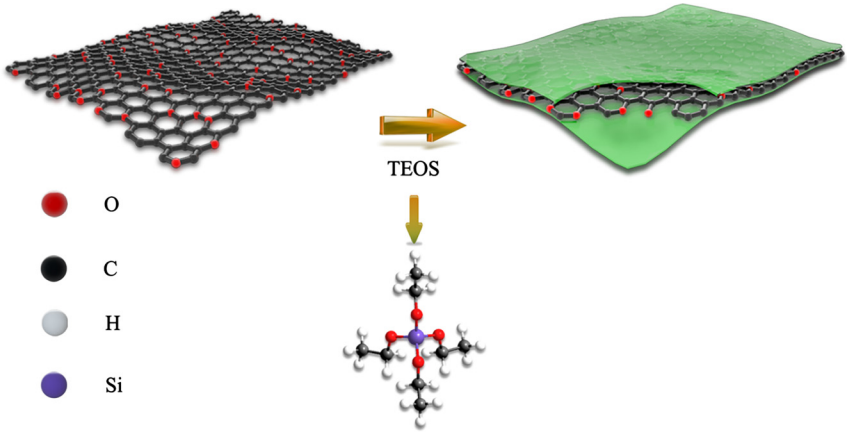

Figure 1: The schematic diagram of the synthesis of SiO_2–GO nanosheets.

Raman spectroscopy and thermogravimetric analysis (TGA). The surface morphology of SiO_2–GO nanosheet was collected by scanning electron microscopy (SEM) and transmission electron microscope (TEM). In addition, the prepared SiO_2–GO nanosheet was dispersed in Zn-EP coatings, becoming the nanofillers. The influence of GO and SiO_2–GO nanosheet on the hydrophobic of the coating surface was measured by the contact angle (CA). The anti-corrosion performance of Zn-EP coating, GO/Zn-EP coating and SiO_2–GO/Zn-EP coating was investigated by Tafel polarisation curve, open-circuit potential (OCP), electrochemical impedance spectroscopy (EIS), salt spray and cathodic delamination tests.

2 Materials and methods

2.1 Materials

Tetrathoxysilane (TEOS, $C_8H_{20}O_4Si$), poly(N-vinyl-2-pyrrolidone) (PVP), ethanol (99.8 wt%), ammonia and acetone were obtained from Chengdu Kelong Chemical Reagent Co. Ltd. Deionized water was made in-house. All chemicals were analytical grade, unless otherwise stated, and used without further purification.

The steel panels (Q235) were purchased from Dehaoke metal material Co. Ltd. The steel panels had dimensions of 60 mm × 40 mm × 1 mm and were polished using 400, 600 and 1000 grade sand papers. They were then decontaminated with dilute hydrochloric acid (5–7 wt%). Epoxy coatings and polyamine hardener were obtained from Beijing Benzema Coatings Co. Ltd.

2.2 Preparation of SiO_2–GO nanocomposite

First, the GO aqueous solution was obtained by modified Hummer's method. Then, SiO_2–GO nanocomposite was synthesized by the sol–gel method. Generally, GO aqueous solution (1% w/v, 4 ml) and PVP (0.4 g) were mixed in ethanol (80 ml), and the mixture ultrasonicated for 1 h at room temperature, with a cycle of 2 s ultrasonication and 2 s pause, giving a total ultrasonication duration of 0.5 h. Then, the compound was magnetically stirring at 40 °C for 30 min. Whilst still stirring, ammonia (4 ml) and TEOS (1 ml) were added to the mixture by micropipette, and the resultant brownish solution refluxed stirring at 40 °C for 12 h with continuously. Subsequently, the compound was repeatedly centrifugated and washed. Finally, the sample was dried at 60 °C for 12 h under vacuum to yield the SiO_2–GO nanocomposite.

2.3 Preparation of GO/Zn-EP and SiO_2–GO/Zn-EP nanocomposite coatings

A series of GO/Zn-EP coatings and SiO_2–GO/Zn-EP coatings with different contents (0.1, 0.5, 1 and 2 wt%) were prepared by the mechanical agitation. Hardener was added prior to coating on the steel substrate. The stoichiometric ratio of Zn-EP coating and curing agent was 5:1 by weight. The coated substrate was cured at 25 °C for 72 h, with the thickness of the coating controlled at 120 ± 5 μm.

2.4 Characterisation of materials

GO and SiO_2–GO were characterised by Fourier transform infrared spectroscopy (FT-IR, EQUINOX-55, Germany) and X-ray diffraction analysis using Cu Kα radiation (XRD, D/Max-3C, Rigaku, Japan), Raman spectroscopy using 532 nm laser excitation (Raman spectrometer, Vantes Co.) was used to detected the crystal structure of GO and SiO_2–GO. Thermal analysis of samples from 30 to 800 °C were recorded on a thermogravimetric analysis (TGA, STA449C, Germany) with a heating rate of 10 K/min. The surface topography and chemical composition of the SiO_2–GO was gathered by field-emission scanning electron microscope (SEM, Zeiss Gemini LEO 1550) and transmission electron microscope (TEM, FEI Tecnai G^2 F20 S-TWIN). The thickness of composites was characterized by atomic force microscope (AFM).

2.5 Coating properties characterisation

2.5.1 Surface morphology characterisation: The coating surface morphology and the dispersion of different fillers in the coating were characterised by scanning electron microscopy (SEM, Zeiss Gemini LEO 1550). The static contact angles of the coating surface hydrophobicity–hydrophilicity were recorded on an OCA 15 plus type contact angle measuring system.

2.5.2 Mechanical properties characterisation: The thickness of the Zn-EP coating was detected by a portable thickness gauge (DUALSCOPE®MPO). The adhesion strength of the Zn-EP composite coatings was implemented on a pull-off adhesion tester (Posi Test AT-A). The impact resistance of the coating was tested by a BEVS impact tester (BEVS1601). The hardness of the coating was recorded on a pencil hardness tester (BEVS 1301). All equipment was purchased from Guangzhou Shenghua Technology Ltd., China.

2.5.3 Electrochemical performance test: The anti-corrosion performance of the GO/Zn-EP and SiO_2–GO/Zn-EP coatings was measured by corrosion weight loss, electrochemical impedance spectroscopy (EIS) and the Tafel polarisation test. The EIS were curve-fitted satisfactorily (errors < 10%) with appropriate equivalent circuits. The corrosion weight loss test was performed in dilute sulphuric acid (20 wt%) for a specific immersion duration, and the rate of corrosion determined by mass loss. A three-electrode system was used to conduct the EIS analysis with saturated Ag/AgCl as the reference electrode, Pt as the counter electrode and coated steel sample as the working electrode, in NaCl aqueous solution (3.5 wt%) as the electrolyte. EIS and potentiodynamic polarisation measurements were recorded on a CHI760E electrochemical workstation (Chenhua, Shanghai). For the EIS measurements, the frequency was kept between 100 kHz and 10 mHz with signal amplitude of 10 mV at OCP. After that, measurements were measured on 1.33 cm^2 of the coating immersed in NaCl solution (3.5 wt %) for different immersion times of 2, 20 or 40 days. Tafel polarisation curves were performed by scanning the electrode potential from −250 to +250 mV at a scanning rate of 1 mV s^{-1}. The measurements were taken three times.

2.5.4 Salt spray test: The salt spray test was used to perform the anti-corrosion performance of the coating. Two scratch lines angled 60° to each other were made in the sample, which was then placed in a salt spray test chamber at an angle of 60°. Atomized NaCl solution (5 wt %, pH 7.0, temperature 37.5 °C) was sprayed on the sample in succession.

3 Results and discussion

3.1 Characterisation of GO and SiO_2–GO

As seen in Figure 2a, a sharp diffraction peak at $2\theta = 10.24°$ can be seen, corresponding to the (001) reflection of GO. For SiO_2–GO sample, an additional diffraction peak appeared at $2\theta = 22.33°$, which is in keeping with the reflection of amorphous silicon (Liu et al. 2015). However, the reflection of GO in SiO_2–GO appeared at $2\theta = 10.41°$, which indicated that the modified GO has good order structure. This shift and the additional peak suggested that SiO_2 was successfully incorporated with the GO (Wan et al. 2014; Yang et al. 2009).

As displayed in Figure 2b, the D and G band intensities increased for SiO_2–GO compared with the original GO. For GO, the G and D bands were at 1580 and 1345 cm^{-1}, severally, and correspond to sp_2-ordered crystalline graphite-like structure and sp_3-disordered carbon structure, severally (Pourhashem et al. 2017). For SiO_2–GO, the G and D bands were at 1623 and 1370 cm^{-1}, severally. A shift to higher wavenumbers indicated GO flakes fall off after embedding silicon dioxide nanometre flakes. These results

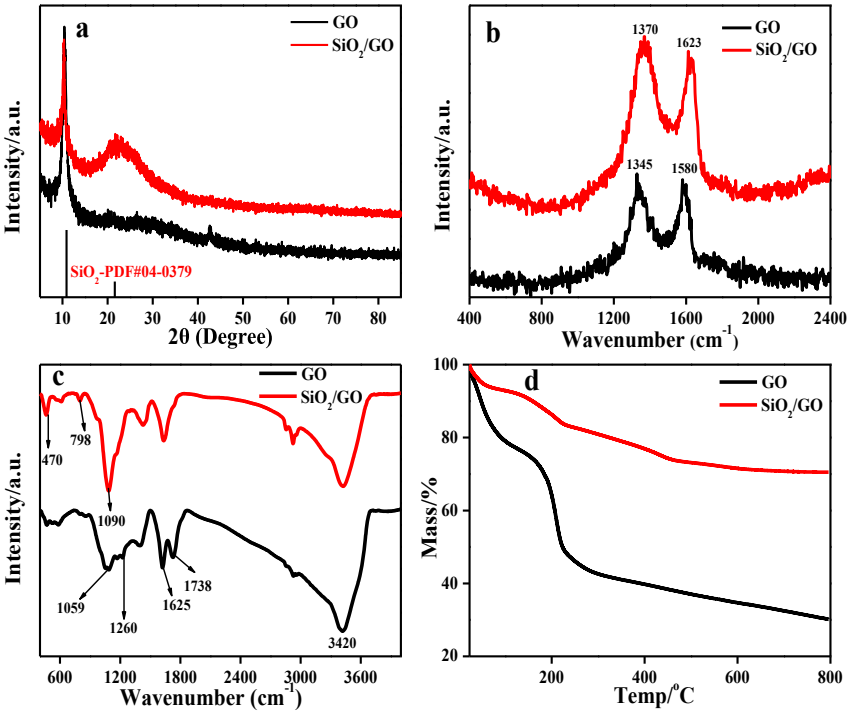

Figure 2: Characterisation of GO and SiO_2–GO by: (a) XRD, (b) Raman spectroscopy, (c) FT-IR and (d) TGA.

provided further evidence for the successful coating of SiO_2 on the GO surface.

As displayed in Figure 2c, the FT-IR spectrum of GO indicates C–OH stretching as a broad peak at 3420 cm^{-1}, C–O stretching of –COOH at 1738 cm^{-1}, C–C skeletal vibrations at 1625 cm^{-1}, O–H vibration of the C–OH groups at 1400 cm^{-1}, and stretching vibration of the epoxy groups at 1059 cm^{-1} (Konios et al. 2014; Parhizkar et al. 2018; Remyamol et al. 2013; Sharif and Gudarzi 2012; Wan et al. 2014; Yang et al. 2009). After the reaction between GO and TEOS, SiO_2–GO showed two new characteristic peaks at 470 and 798 cm^{-1}, which were due to Si–O–Si bending vibration and Si–OH stretching, severally (Kathi and Rhee 2008). In addition, the peak at 1090 cm^{-1} was attributed to the Si–O–C asymmetric stretching vibration (Zhu et al. 2012); this peak was intense, indicating that the –OH of GO reaction with the $-OC_2H_5$ of TEOS promotes non-covalent interactions. Furthermore, the Si–O–C bands indicated that the Si–OH group produced by the hydrolysis of TEOS has been bonded to the GO surface.

TGA was performed to quantitatively analyse the SiO_2–GO, and the results are shown in Figure 2d. At approximately 100 °C, the weight of GO decreased by about 21%, possibly because of the water loss. The weight of GO decreased by 31% at 100–230 °C, possibly from removal of the oxygenated functional groups of GO (Zhang and Choi 2012). SiO_2–GO had less loss of mass (24 wt% total), because of SiO_2's superior thermal stability and resistance to high temperature. Furthermore, the weight decrease of SiO_2–GO occurred at 250–500 °C, which was likely due to the oxidative thermal decomposition of incompletely reacted TEOS. Previous research has shown that, when using silane coupling agents to modify certain carbon materials, silane groups are formed, thereby improving the thermal stability of the materials (Becerril et al. 2008). All of these results demonstrated that SiO_2 was effectively functionalised onto the GO sheets.

The morphology and microstructure of the prepared SiO_2–GO nanosheets were carried out by SEM. Figure 3a clearly depicts the blocky structure in a low magnification and wrinkle structure in a high magnification of the GO, which is the characteristic morphology of GO (Dhawade and Jagtap 2012). In Figure 3b, many free-standing sheets about 500 nm to several micrometres similar to the morphology of GO were observed in a low magnification. In addition, there were no dissociative silica particles or pristine GO flakes in Figure 3a. This suggested that silica was successfully coated on the GO flakes' surface. Elemental mapping of carbon, silicon and oxygen in SiO_2–GO flakes can further determine the nature of the structure (Figure 3c–e), which revealed the homogenous dispersion of C, Si and O in the SiO_2–GO sheets.

Figure 4 demonstrates the TEM and AFM images of GO and SiO_2–GO. In Figure 4a, the GO has a transparent lamellar structure and obvious folds at the edge of the GO sheets, which corresponds to the SEM diagram of GO. For Figure 4d, the surface was covered with a thick film, this mainly due to the SiO_2 produced by hydrolysis of TEOS was

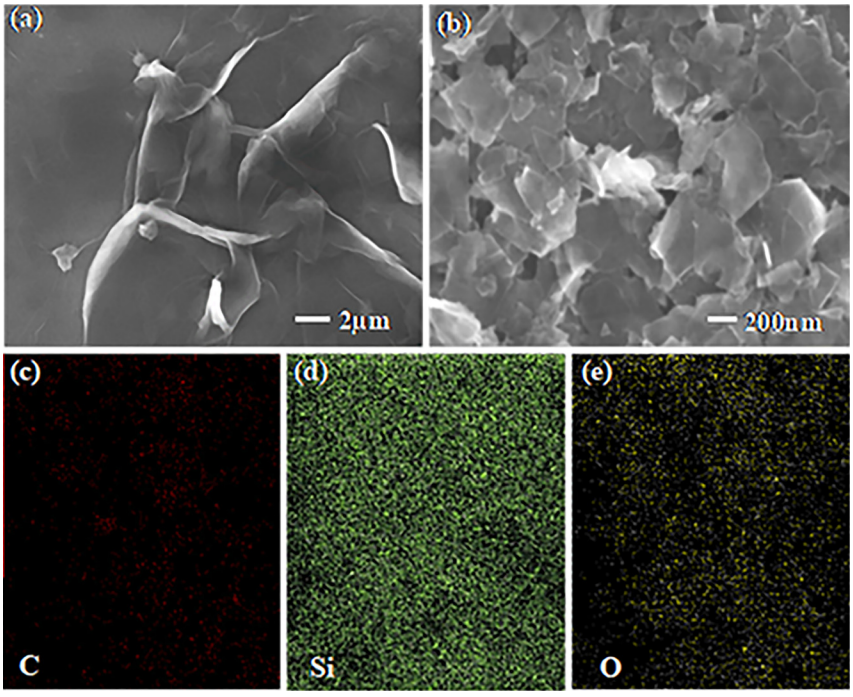

Figure 3: Typical scanning electron microscopy (SEM) images of the GO (a) and SiO_2–GO (b); elemental mapping images of SiO_2–GO sheets: (c) C, (d) Si and (e) O.

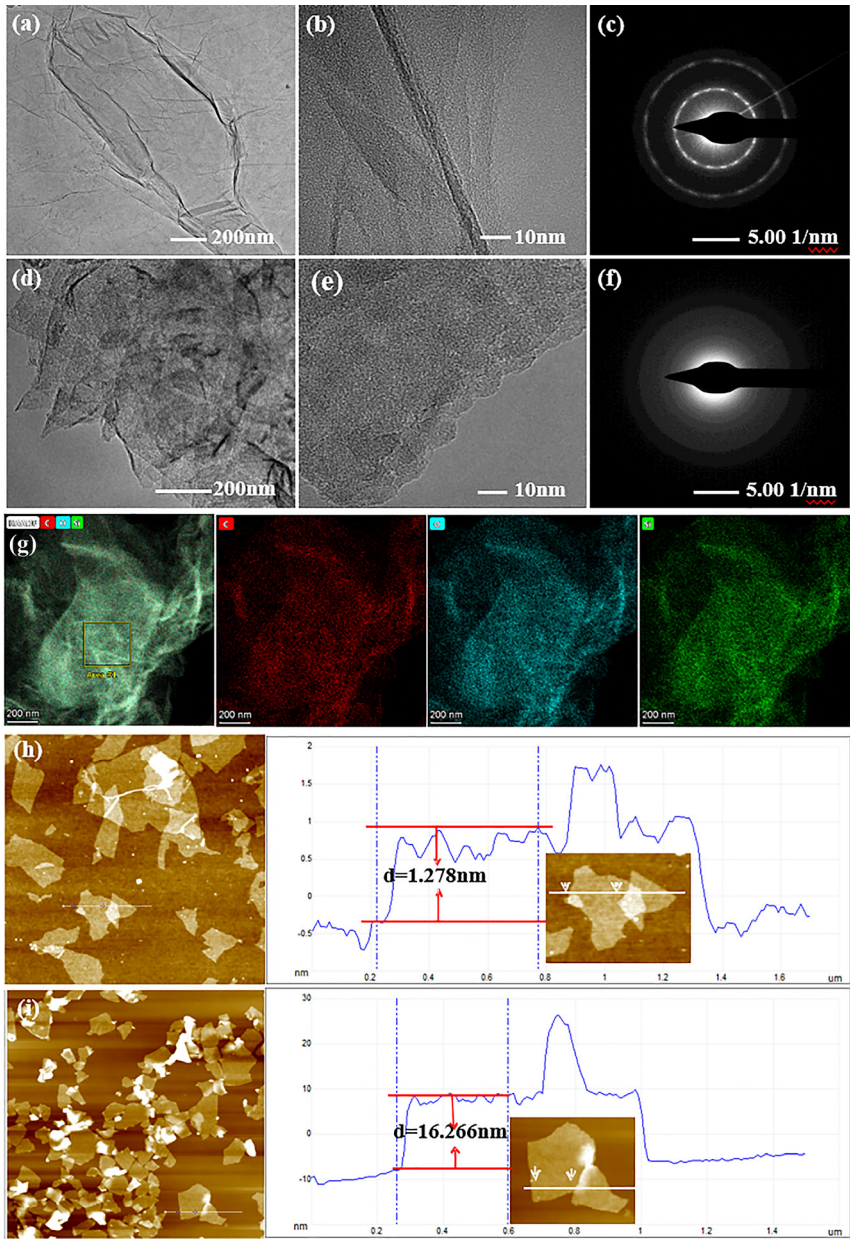

Figure 4: Typical transmission electron microscope (TEM) and atomic force microscope (AFM) images of: (a) low magnification and (b) high magnification of GO, (d) low magnification and (e) high magnification of SiO_2–GO; (c) and (f) was the electron diffraction patterns of GO and SiO_2–GO, respectively; (g) Dark-field TEM image and corresponding mapping images for C, O and Si elements of SiO_2–GO; (h) and (i) was the AFM image of GO and SiO_2–GO, respectively.

indeed attached to the surface of GO. Meanwhile, there were no dissociative silica particles or pristine GO flakes. From Figure 4b and d, the thickness of the SiO_2–GO nanosheets is about 10 nm, which is significantly thicker than the film thickness of the GO. In Figure 4j, it can be seen from the elemental mapping images that the C, O and Si elements of SiO_2–GO are uniformly distributed, respectively. At the same time, the electron diffraction patterns of GO and SiO_2–GO can also provide strong evidence that the synthesized SiO_2–GO nanosheets is a two-dimensional nanoflake structure. The AFM analysis also was obtained, suggesting that the average thickness of SiO_2–GO was 16.266 ± 0.5 nm. The higher thickness of SiO_2–GO sample compared to GO sheets (1.278 ± 0.2 nm) represents that SiO_2 have uniformly covered the surface of GO sheets.

3.2 Morphology analysis of the coating

To observe the dispersity and interface reaction of nanofillers on the substrates, the surface morphology and the cross-sectional morphology of the pure Zn-EP, GO/Zn-EP and SiO_2–GO/Zn-EP coatings on steel matrix were collected by SEM (Figure 5). The surface structure and the cross section morphology of Zn-EP coating is demonstrated in Figure 5a_1. Many grainy zinc powder was obviously seen in the coating,

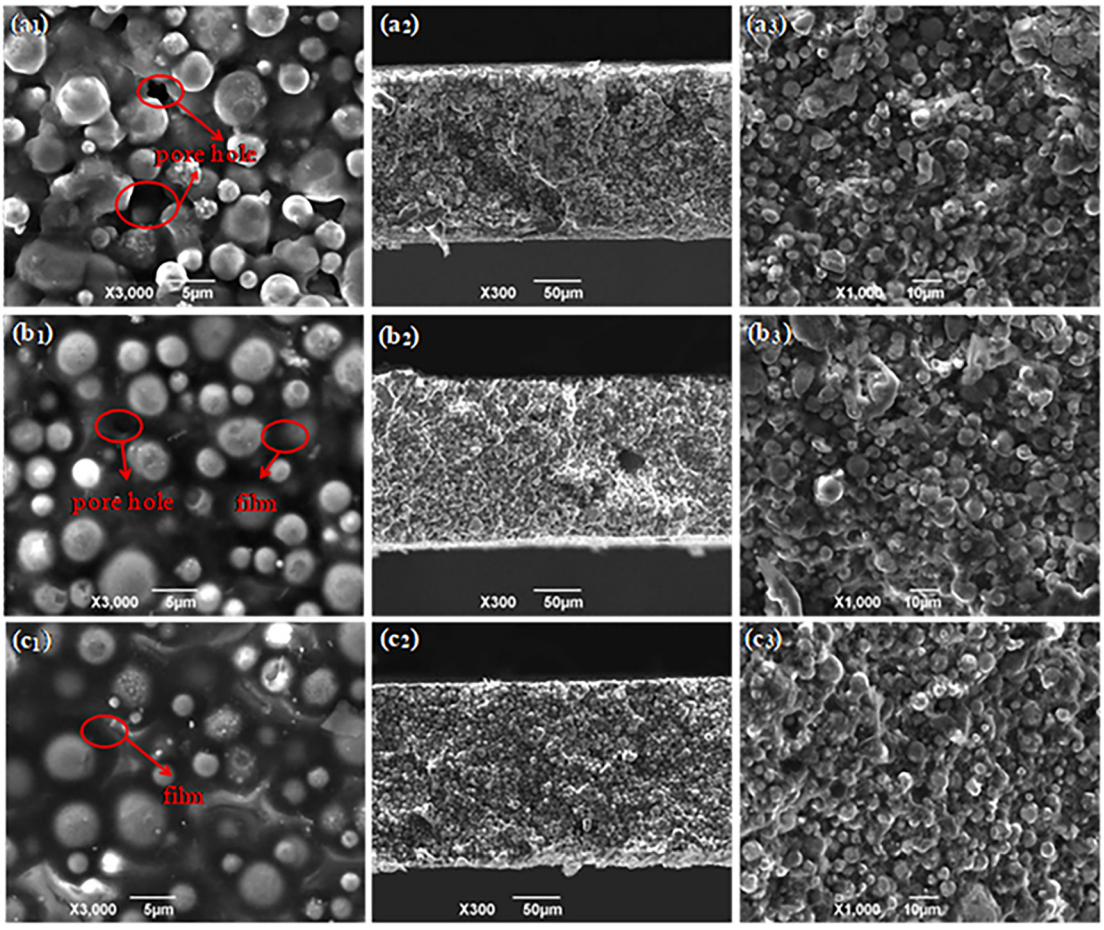

Figure 5: SEM images of the surface morphology of: (a_1) pure Zn-EP, (b_1) 0.5 wt% GO/Zn-EP , and (c_1) 0.5 wt% SiO_2–GO/Zn-EP nanocomposite coatings; the cross-sectional morphology with different magnification of (a_2, a_3) pure Zn-EP, (b_2, b_3) 0.5 wt% GO/Zn-EP and (c_2, c_3) 0.5 wt% SiO_2–GO/Zn-EP nanocomposites coatings.

which led to numerous inevitable holes and cracks on the coating. It has been marked with a red circle in the Figure (a_1. These unavoidable defects can affect the cathodic protection and coating property of zinc powder. In Figure 5b_1, b_2, b_3, the number of pores on the GO/Zn-EP coating were obviously reduced and the internal structure of the coating more compact. Figure 5c_1, c_2, c_3 shows the smooth surface structure and internal structure of the SiO_2–GO/Zn-EP coating, arising from its homogeneous dispersion and being well-embedded in the Zn-EP coating via strong interface interaction between the polymer substrate and Si–OH bonds of the SiO_2–GO nanosheets. This indicated that the SiO_2–GO nanosheets have a good compatibility with the coatings. Results show that the addition of SiO_2–GO nanosheets could effectively improve the defects of the coating itself and greatly prolong the corrosion paths of the corrosive medium to the matrix, hence effectively improving the protective properties of the steel substrate.

3.3 Mechanical properties of coatings

The protective properties of a coating are determined by its impermeability. In general, the higher the impermeability of the coating, the better its performance in metal protection. In order to ensure that the coating could provide a good physical isolation layer for the steel substrate against corrosive substances from the external environment, the coating must have sufficient adhesion strength (Treossi et al. 2009). As seen in Figure 6a and Table 1, the adhesion force of the coating varied with the amount of GO and SiO_2–GO. Adhesion force reached a maximum when the amount of GO or SiO_2–GO was 0.5 wt%, which was because the large surface area and excellent mechanical performance of the nanofillers could effectively compensate for defects arising from the loose structure of the Zn-EP coating surface (Dong and Liu 2016). At the same time, Figure 6b and c indicates that SiO_2–GO nanoflakes also have a crucial

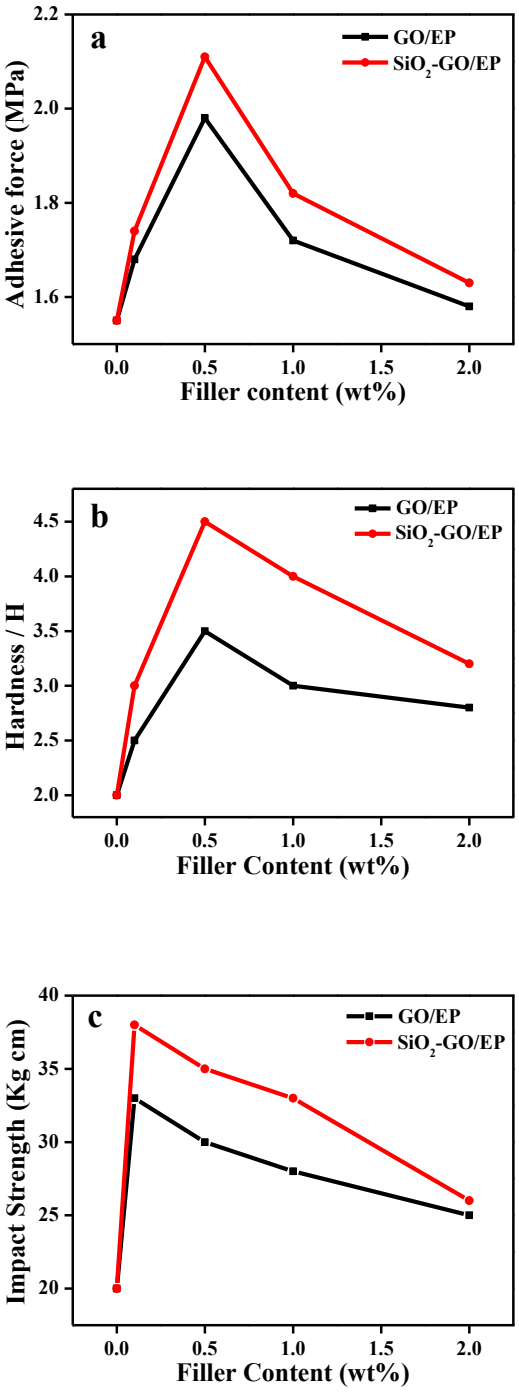

Figure 6: The (a) adhesion, (b) hardness and (c) impact strength of pure epoxy coating and its composites with different filler loadings.

influence on the hardness and impact strength of the samples. This was mainly due to the fact that SiO_2–GO nanosheets with three-dimensional network structure can increase the cross-linking density with the polar groups in the Zn-EP coating. Because SiO_2 has a large specific surface area, and after being compounded with GO, the SiO_2–GO surface carries an active group-silicon hydroxyl group, which strongly interacts with the ether bond or epoxy group in the matrix. It forms a good interfacial bond between the inorganic phase and the organic phase, thereby increasing the cross-linking density with the polar groups in the Zn-EP coating and increasing the interfacial bonding force of the two phases. The results demonstrate that the addition of SiO_2–GO can enhance the absorption and adhesion of the coatings (Dashtizadeh et al. 2011). However, the adhesion, hardness and impact strength of the coatings decreased rapidly when the content of filler was further increased, which might be due to agglomeration resulted from the uneven dispersion of nanofillers in the coating, so then cannot perform their excellent mechanical properties.

Table 1: Adhesion test of pure epoxy coating and Zn-EP composite coating.

Content (wt%)	Coating	Pressure (MPa)	Duration time (s)	Dolly (mm)	Rate (MPa/s)	Result
0	GO	1.55	6.5	20	0.20	Pulled
	SiO_2/GO	1.55	6.5	20	0.20	Pulled
0.1	GO	1.68	6.8	20	0.20	Pulled
	SiO_2/GO	1.74	7.3	20	0.20	Pulled
0.5	GO	1.98	8.2	20	0.20	Pulled
	SiO_2/GO	2.11	9.7	20	0.20	Pulled
1	GO	1.72	7.0	20	0.20	Pulled
	SiO_2/GO	1.82	7.6	20	0.20	Pulled
2	GO	1.58	6.6	20	0.20	Pulled
	SiO_2/GO	1.63	6.9	20	0.20	Pulled

3.4 Corrosion resistance performance of the coating

3.4.1 Contact angle test

The most intuitive method for evaluating the hydrophobicity of the coating is the CA test. Water was used as solvent to calculate contact angle of sample. Young and Neumann equations (Gao et al. 2008) (Eqs. (1) and (2) below, respectively), were utilised to calculate the work of adhesion (W_A) and surface free energy of the film (γ_{sv}), where γ_{lv} is the surface tension of water (γ_{lv} = 7.28 μJ/cm^2), θ is the contact angle of water and β is 0.01247 ± 0.0010 (μJ/cm^2)$^{-2}$. CA, W_A and γ_{sv} values for diverse samples are shown in Figure 7.

$$W_A = \gamma_{lv}(1 + \cos\theta) \quad (1)$$

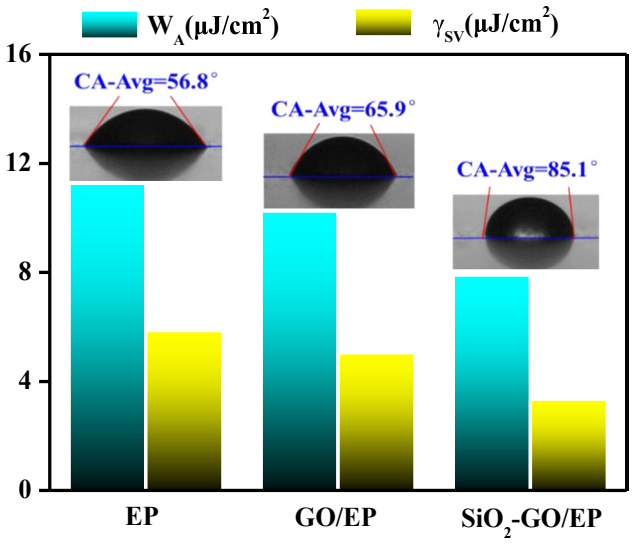

Figure 7: Contact angle measurements results, work of adhesion and surface free energy results for Zn-EP, GO/Zn-EP and SiO_2–GO/Zn-EP coatings.

$$W_A = 2(\gamma_{lv}\gamma_{sv})^{1/2} \exp\left[-\beta(\gamma_{lv} - \gamma_{sv})^2\right] \quad (2)$$

From Figure 7, a change of CA of GO/Zn-EP and SiO_2–GO/Zn-EP coatings compared with EP coating can clearly be observed. There was a marked increase in CA of the coating when 0.5 wt% GO or SiO_2–GO nanosheets was added into the Zn-EP matrix; this increase was greatest for the SiO_2–GO/Zn-EP coating where the CA increased from 56.8 to 85.1°. SiO_2–GO increase the water contact angle on coatings because it decreases the hydrophilicity of coatings and leads to decrease of water absorption on Zn-EP coatings. This showed that the SiO_2–GO/Zn-EP coating surface has good hydrophobicity and barrier performance. In Figure 7, W_A and γ_{sv} decrease markedly for the 0.5 wt% SiO_2–GO/Zn-EP coating, which indicated that the corrosive substances were difficult to stay on the surface of the coating, so it has a good protective effect on the steel substrate (Zaslavsky et al. 1990). Therefore, addition of an appropriate amount of SiO_2–GO to the Zn-EP coating could lengthen the diffusion path of the corrosive species and thereby significantly improve its corrosion-protective properties.

3.4.2 Corrosion weight loss test

Figure 8 depicts the impact of 0.5 wt% GO or SiO_2–GO composites on the acid anticorrosion performance of the Zn-EP coating. Different coatings and steel substrates were dipped into 20 wt% sulphuric acid solution, and the anti-corrosion performance of the Zn-EP coatings was estimated

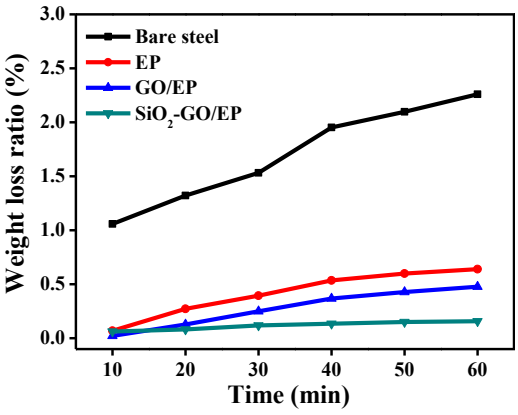

Figure 8: Corrosion weight loss ratio curves of the bare steel and various coating samples.

by the rate of weight loss. As seen in Figure 8, the weight loss rate increased with increased soaking time of the coatings. After immersion for 60 min, for the bare steel without any protection, the weight loss rate was as high as 2.25%. For the Zn-EP coating, the weight loss rate decreased to 0.64%, which indicated that the protective current produced by the dissolution of zinc powder in the coating inhibited the corrosion of the steel surface. By comparison, the corrosion weight loss rates for samples with GO and SiO_2–GO coating were 0.48 and 0.15%, respectively. This result demonstrated that the GO and SiO_2–GO nanosheet could formed a dense network structure with epoxy groups, which reduced the dissolution of zinc powder and prolong the transport path if corrosive medium, thus effectively protects the steel substrate from being eroded.

3.4.3 Tafel polarisation measurements

The corrosion resistance of Zn-EP coating with or without GO and SiO_2–GO was studied by electrochemical measurements (Lu et al. 2017). Figure 9 depicts the Tafel polarisation plots for bare steel and sample with the three coating systems. Corrosion potential (E_{corr}), corrosion current density (I_{corr}) and corrosion protection efficiency (CPE) were derived from Table 2. In this study, the I_{corr} was gathered from the Tafel plot by extending a straight line along the linear portion of the cathodic or anodic plot and by extrapolating it to the E_{corr} axis. CPE was used to compare the protective effect of GO/Zn-EP coating and SiO_2–GO/Zn-EP coating on steel substrate. The CPE was calculated using the following Eq. (3), where I^0_{corr} is the corrosion current (μA/cm^2) of bare steel, and I^c_{corr} is the corrosion current (μA/cm^2) of the coated specimen (Mo et al. 2015):

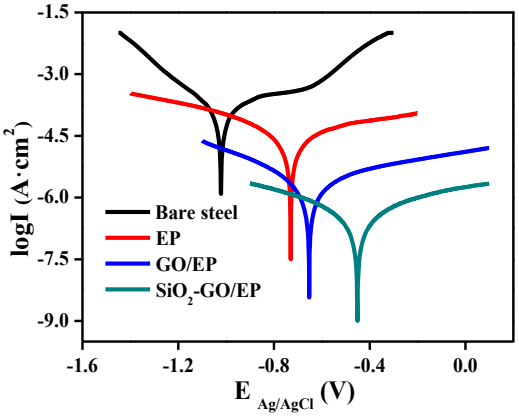

Figure 9: Tafel plots for bare steel, Zn-EP-, GO/Zn-EP- and SiO_2–GO/Zn-EP-coated samples after immersion in 3.5 wt% NaCl solution for 48 h.

$$\mathrm{CPE}(\%) = \frac{I^0_{\mathrm{corr}} - I^{\mathrm{c}}_{\mathrm{corr}}}{I^0_{\mathrm{corr}}} \times 100\% \tag{3}$$

Generally, low I_{corr} and high E_{corr}, CPE indicates greater corrosion protection. As seen in Figure 9, the coated sample exhibited higher positive corrosion potential than does the bare steel sample. The hyperbolic plot shifts towards a lower current density indicated that the anti-corrosion performance increase with the addition of GO and SiO_2–GO.

As shown in Table 2, the i_{corr} (127.800 μA) of the bare steel substrate was far higher than that of the i_{corr} (16.750 μA) of Zn-EP-coated substrate, which indicated the protective effect of the Zn-EP coating. Incorporation of GO and SiO_2–GO nanofillers into the Zn-EP substrate lead to crucial reduction of the i_{corr} and an appreciable increase of the CPE from 86.98% for the EP-coated substrate to 98.85 and 99.55% for GO and SiO_2–GO, respectively. This was mainly due to the barrier properties provided by GO and SiO_2–GO. Additionally, for the SiO_2–GO/Zn-EP coating the i_{corr} decreased to 0.561 μA (compared with 16.750 μA for the EP coating), accompanied by the highest CPE value. The low i_{corr} and high CPE indicated the superior barrier ability of this coating because of its hydrophobicity, which can hinder the permeation of corrosive species and provides unexceptionable corrosion resistance properties (Chang et al. 2014).

The polarisation resistance (R_p) was related to the corrosion current density I_{corr}, through the Stern–Geary equation:

$$I_{\mathrm{corr}} = \frac{\beta_a \beta_c}{2.303(\beta_c - \beta_a)R_p} \tag{4}$$

where β_a and β_c are, respectively, the anodic and cathodic Tafel slopes.

It was found that the R_p of the GO/Zn-EP coating was 30.825 kΩ cm^2, about five times higher than for the EP coating (2.869 kΩ cm^2). The increase on account of the physical barrier properties offered by the appearance of GO sheets in the sample. Compared with the Zn-EP and GO/Zn-EP coatings, the hydrophobic SiO_2–GO/Zn-EP coating had the highest R_p value (78.031 MΩ cm^2), which indicated that the SiO_2–GO film could be used as a physical isolation layer to impede the transmission of corrosion media to the interface of the coating and metal and there by enhance the corrosion resistance of the sample (Syed et al. 2017).

With extended immersion time, the impedance spectra changed markedly for all of coatings, and the R_p values for all the samples were greatly reduced. These phenomena were due to penetration of corrosive species and dissolved oxygen to the interface of the coating and metal. However, compared with the Zn-EP and GO/Zn-EP coatings, the SiO_2–GO/Zn-EP coating still maintained a relatively high R_p value. This demonstrated that use of SiO_2–GO nanoflakes could increase the physical barrier and anti-corrosion performance of the metal coating.

3.4.4 EIS measurements

EIS was obtained with an efficient way to estimate the anti-corrosion performance of the coatings. The anti-corrosion properties of diverse samples could be calculated by fitting the EIS data using equivalent circuits, which can provide selective information about the coating corrosion (Bahlakeh et al. 2017). Nyquist and Bode diagrams are offered in Figure 10.

Table 2: Potentiodynamic polarisation parameters.

Coating system	E_{corr} (mV)	i_{corr} (μA cm^{-2})	β_c (mV dec^{-1})	β_a (mV dec^{-1})	R_p (kΩ)	Corrosion protection efficiency (CPE) (%)
Bare steel	−1021	127.800	5.244	3.573	0.3858	/
EP coating	−730	16.750	4.813	4.231	2.869	86.89
GO/EP coating	−624	1.461	5.062	4.592	30.825	98.85
SiO_2–GO/EP coating	−451	0.561	5.048	4.886	78.031	99.55

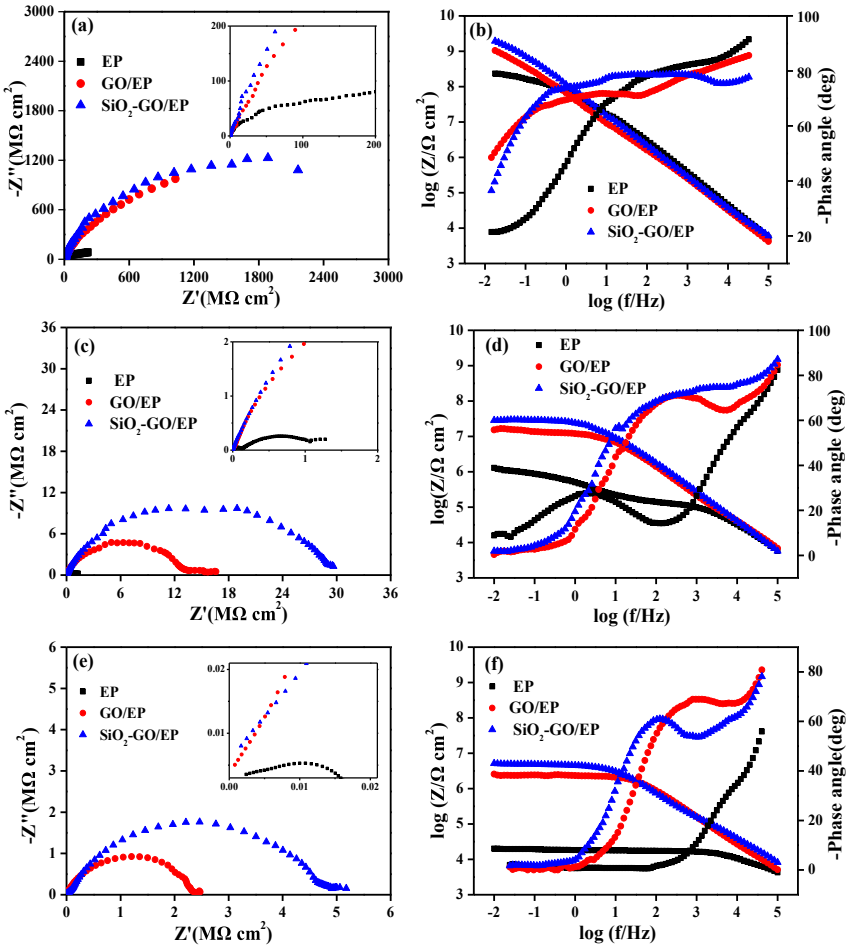

Figure 10: Nyquist and Bode diagrams of the Zn-EP EP, GO/Zn-EP and SiO_2–GO/Zn-EP samples immersed in 3.5 wt% NaCl solution for (a) and (b) 2 days, (c) and (d) 20 days and (e) and (f) 40 days; (a), (c) and (e) are Nyquist diagrams, (b), (d) and (f) are Bode diagrams.

The Nyquist and Bode plots of the Zn-EP, GO/Zn-EP and SiO_2–GO/Zn-EP samples immersed for 2, 20 and 40 days in 3.5 wt% NaCl solution are exhibited in Figure 10. The inset of Figure 10a demonstrates that the absolute impedance of the SiO_2–GO/Zn-EP coating was increased compared with the GO/Zn-EP and Zn-EP coating samples. Figure 10b also shows that only one relaxation time could be found in the Bode diagrams of all coatings after 2 days immersion, which could be ascribed to the dielectric capacity of the polymeric coating which slows the corrosion of the metal surface (Ramezanzadeh et al. 2016a,b,c). In the initial immersion stage, the zinc powder in the coating could be used as a protective layer to stop corrosion medium from infiltrating in to the coating. This corrosion process could be simulated by the equivalent circuit of Figure 11a. In the equivalent circuit, R_s was the solution resistance, R_c was the coating resistance, CPE_c was the coating constant phase element, R_{ct} was the charge transfer resistance of electrochemical reaction in the metal/coating interface, and CPE_{dl} was the double layer constant phase element.

However, coating barrier performance declined as immersion time increased. After immersion in 3.5 wt%

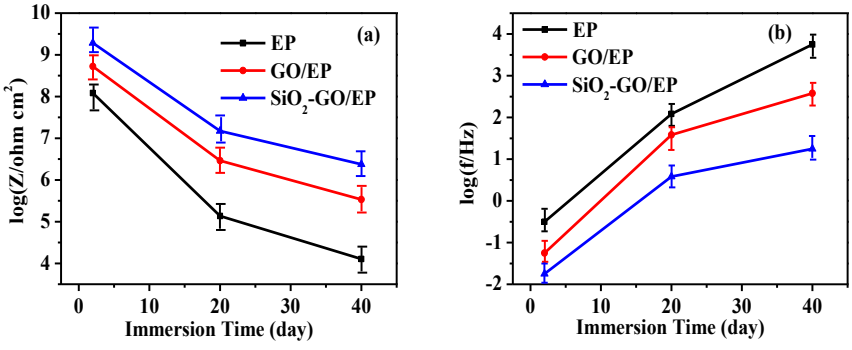

Figure 11: Electrochemical parameters extracted from Bode plots of the Zn-EP, 0.5 wt% GO/Zn-EP and 0.5 wt% SiO_2–GO/Zn-EP samples immersed in 3.5 wt% NaCl solution for 2, 20 and 40 days.

NaCl solution for 20 days, two time constants could be seen in the Bode diagrams (Figure 10d) of Zn-EP and GO/Zn-EP coatings. At the same time, the impedance of the Zn-EP coating reduced obvious in Figure 10c. This was mainly because of the porous structure of the Zn-EP coating and the dissolution of zinc powder, which lead to the reduced of contact between zinc particles, and therefore gave rise to evident weakening of cathodic protection. For the GO/Zn-EP coating and SiO_2–GO/Zn-EP coating, the coating still maintains a relatively high impedance value in the middle of the immersion. This indicated that the corrosive medium was only in contact with zinc, and then corrosion products were formed to fill the microporous defect in the zinc-rich layer. Moreover, the oxide formed passivation layer with the lamellar GO and SiO_2–GO, which prevented the corrosive medium from penetrating to the surface of the steel matrix.

With further increase in immersion time, the Zn-EP coating showed one time constant in the Bode plot of Figure 10f. However, in Figure 10e Nyquist plot, two capacitive arcs corresponding to directly corrosion on the surface of the metal were observed, and thus some corrosive products appeared under the coating. In fact, some corrosive electrolyte has been penetrated into the coating substrate through micro-pores and defects on the Zn-EP coating surface, resulting in damage to the coating and in reducing the barrier performance (Hassan 2007). For GO/Zn-EP and SiO_2–GO/Zn-EP, two time constants could still be seen in Figure 10f. The coating behaviour with diverse frequency range was mostly resistive, and the capacitive behaviours could be observed only under the high frequency. The results reveal that the coating deterioration and destruction of interfacial adhesion bonds, allowing corrosion agents to penetrate beneath the coating.

To quantitatively evaluate the barrier performance of the coatings and their active corrosion resistance performance, impedance spectra used to simulate the corrosion behaviour of the coated substrates were fitted to the corresponding equivalent circuit in Figure 12 (Ozyılmaz et al. 2006). Figure 12a and b was used to fit the EIS results with two time constants. In the equivalent circuit, R_s was the solution resistance, R_c was the coating resistance, CPE_c was the coating constant phase element, R_{ct} was the charge transfer resistance of electrochemical reaction in the metal/coating interface, and CPE_{dl} was the double layer constant phase element, and W is the Warburg impedance relevant to the diffusion process.

Generally, barrier ability of the coating was demonstrated by R_c and CPE_c. From Figure 11 and Table 3, increased immersion time resulted in a decrease of $|Z|_{0.01Hz}$ and R_c for all coatings, which indicated that the coating

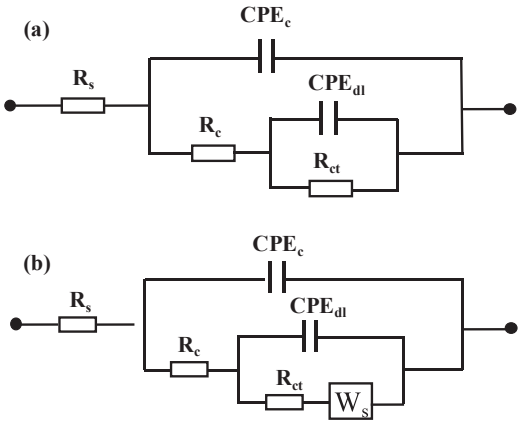

Figure 12: The proposed equivalent circuit model for numerical simulation of EIS data presented in Figure 10. (a) the GO/Zn-EP and SiO_2–GO/Zn-EP samples immersed in 3.5 wt% NaCl solution with the 2, 20 and 40 days and (b) other coupon.

surface has been damaged. At the beginning of immersion, the Zn-EP coating showed low R_c and high CPE_c, which arose from rapid diffusion of the electrolyte solution due to Zn-EP coating hydrophilicity. In contrast, for GO/Zn-EP and SiO_2–GO/Zn-EP coatings, the R_c values increased (from 8.20 MΩ cm^2 for the Zn-EP coating) to 1060 and 1760 MΩ cm^2, with low CPE_c values. The high R_c and low CPE_c values indicated the preferable barrier ability of the GO/Zn-EP and SiO_2–GO/Zn-EP coatings, which prevented the permeation of corrosive species and provided outstanding corrosion protection. From Figure 10 and Table 3, the diagrams with GO/EP and SiO_2–GO/EP coatings have no Warburg impedance, indicating that the corrosion mechanism was changed with the addition of GO/Zn-EP and SiO_2–GO/Zn-EP to the coating (Chang et al. 2012).

In summary, the failure procedure of the coating mainly includes the following three steps:

– The permeation stage of the corrosive medium. The rapid decrease of R_c at the initial stage of the experiment was mainly because of the diffusion of corrosion medium through the microporous structure of the coating surface. The transmission speed of the corrosive species to the coating/metal interface and the concentration of dissolved oxygen at the interface increased continuously, resulting in the coating's rapid decrease in R_c and rapid increase in capacitance. Additionally, penetration of the corrosive species accelerated the cathodic reduction reaction rate on the metal surface, enhancing the cathodic delamination procedure and therefore increasing the active area, further accelerating the decline in the corrosion resistance of the coating.

Table 3: Electrochemical parameters from the impedance plots for Zn-EP, 0.5 wt% GO/Zn-EP and 0.5 wt% SiO_2–GO/Zn-EP immersed in 3.5 wt % NaCl solution for different immersion times; data were normalised with respect to total area (1.33 cm^2) and the values are the mean of three replicates.

Samples	R_s (Ω cm^2)	R_c (MΩ cm^2)	CPE_c		R_{ct} (MΩ cm^2)	CPE_{dl}		W_s (Ω^{-1} cm^{-2} s^n)
			Y_o (Ω^{-1} cm^{-2} s^n)	n		Y_o (Ω^{-1} cm^{-2} s^n)	n	
Zn-EP(2d)	189	8.20	7.88×10^{-10}	0.926	213	2.98×10^{-9}	0.523	2.94×10^{-8}
Zn-EP(20d)	450	0.120	3.13×10^{-9}	0.820	1.07	6.56×10^{-7}	0.576	3.46×10^{-5}
Zn-EP(40d)	68.3	0.0179	3.09×10^{-8}	0.667	0.00157	4.01×10^{-4}	0.725	4.70×10^{-3}
GO/Zn-EP(2d)	270	1060	3.26×10^{-9}	0.828	1580	4.2×10^{-9}	0.791	–
GO/Zn-EP(20d)	270	5.19	3.46×10^{-8}	0.662	8.94	3.0×10^{-9}	0.867	–
GO/Zn-EP(40d)	360	1.15	1.12×10^{-8}	0.813	1.27	1.25×10^{-8}	0.766	–
SiO_2–GO/Zn-EP(2d)	405	1760	1.71×10^{-9}	0.87	2320	2.39×10^{-9}	0.725	–
SiO_2–GO/Zn-EP(20d)	270	11.9	2.51×10^{-9}	0.831	17.4	3.16×10^{-9}	0.693	–
SiO_2–GO/Zn-EP(40d)	270	3.02	3.03×10^{-8}	0.613	1.97	5.98×10^{-9}	1.030	–

- The corrosion stage of the interface metal. The electrochemical reaction area enlarged continuously with the persistent penetration of corrosive media through the coating. Abundant corrosion products accumulated at the interface of the coating and metal when the electrochemical reaction reached a certain extent; these corrosion products hindered the diffusion of corrosive species and reduced the rate of decline of the coating performance.
- The failure stage of the coating. As the immersion time increased, accumulated corrosion products were gradually dissolved by penetration of the corrosive electrolyte. This led to decreased bonding force between the coating and metal interface and the coating flaking off. In addition, R_c dropped significantly and the coating capacitance increased rapidly. At this point, the protective impact of the coating was completely lost.

3.4.5 Salt spray test results

The effects of incorporation of GO and SiO_2–GO into the Zn-EP coating on the anti-corrosion performance of the composite coatings were obtained by the salt spray test and electrochemical measurements. Images of the different samples following exposure to salt fog box for 360 h are demonstrated in Figure 13.

Figure 13 reveals that several obvious corrosions were produced around the scratch and under the coating, suggesting the poor anti-corrosion properties of the coating. After the 360 h salt spray test, many bubbles and corrosion spots came out on the Zn-EP coating surface (Figure 13a). The incorporation of GO to the Zn-EP coating contributed to a sharp decrease in the amount of corrosion around the scratch and under the coating. However, it reveals that the increase of SiO_2–GO nanoflakes to the coating led to a very great reduction in corrosion, especially beneath the coating. Compared with the SiO_2–GO/Zn-EP coating, the Zn-EP and GO/Zn-EP coatings had a lot of corrosion products, which indicated that corrosive electrolytes had reached the coating-steel interface. These results demonstrated that increase of SiO_2–GO to the Zn-EP coating aggrandized its barrier and anti-corrosion performance to a greater extent than for the GO/Zn-EP coating.

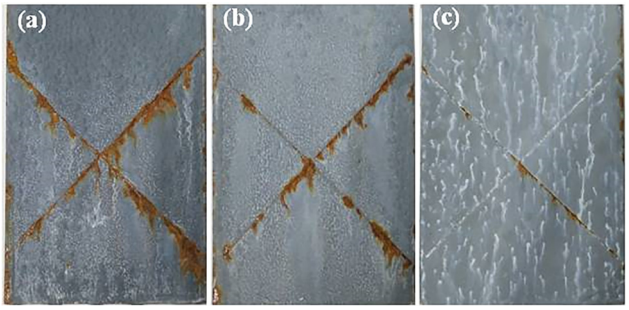

Figure 13: Visual performances of the: (a) Zn-EP, (b) GO/Zn-EP and (c) SiO_2–GO/Zn-EP coatings exposed to the salt spray test for 360 h.

3.4.6 Peel adhesion test

The peel off adhesion strengths of the Zn-EP, GO/Zn-EP and SiO_2–GO/Zn-EP coatings were measured using the pull-off test. Following exposure to continuous spray for 360 h in a salt fog box with 3.5% NaCl solution, adhesion loss rate (A_{loss}) values were obtained on the basis of Eq. (5). The adhesion strength and adhesion loss values of diverse samples are compared in Table 4 and Figure 14. The dry adhesion strength (A_1) refers to the adhesion strength of the coating after drying; the peel off adhesion strength (A_2) refers to the adhesion strength of the coating after continuous spray for 360 h in a salt fog box.

Table 4: Adhesion force values obtained from 3.5% NaCl solution pull-off test (adhesion was measured before and after the test) for the Zn-EP, GO/Zn-EP and SiO_2–GO/Zn-EP coatings.

Sample coating	A_1 (MPa)	A_2 (MPa)	A_{loss} (%)
Zn-EP coating	1.55	0.49	68.38
GO/Zn-EP coating	1.98	0.83	58.08
SiO_2–GO/Zn-EP coating	2.11	1.23	41.7

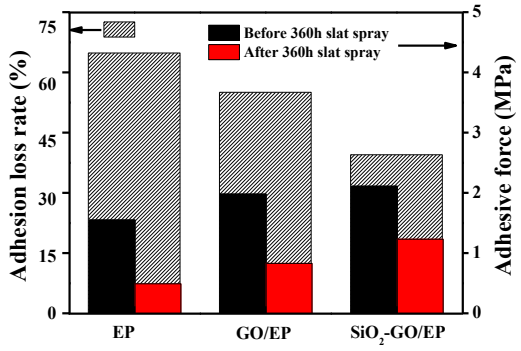

Figure 14: Adhesion force of the coatings before and after exposure to salt spray fog for 360 h.

$$(A_{loss}\%) = \frac{(A_1 - A_2)}{A_1} \quad (5)$$

Table 4 indicates that the increase of GO and SiO_2–GO nanosheets directly affects the dry adhesion strength of the coating. Incorporation of SiO_2–GO nanosheets into the Zn-EP coating led to a sharp rise in coating adhesion to the steel matrix. From Figure 14, the adhesion strength of the Zn-EP coating decreased approximately threefold and GO/Zn-EP coating declined approximately twofold after the peel adhesion test. However, the adhesion loss rate declined sharply after the increase of SiO_2–GO nanoflakes into the coating, due to the hydrophobic surface of this coating and its physical isolation effect, blocking the diffusion of corrosive electrolyte to the interface of the coating and metal.

3.4.7 Corrosion protection mechanism of SiO_2–GO/Zn-EP coating

All the above results show that covalent functionalisation of GO nanoflakes with silane led to a high degree of GO sheet dispersion and intercalation in the Zn-EP substrate, which primely enhanced the barrier performance and anti-corrosion performance of the Zn-EP coating. The corrosion of the metal substrate surface coating undergoes three stages including water absorption, diffusion of corrosive agents and corrosive ions reaching the interface of the coating and metal. Corrosion occurs when corrosive substances reach metal surface, which incorporates numerous redox reactions. The corrosion process and rust formation are explained by the following equations:

$$Fe - 2e^- \rightarrow Fe^{2+} \quad (6)$$

$$Fe^{2+} - e^- \rightarrow Fe^{3+} \quad (7)$$

$$O_2(g) + 2H_2O + 4e^- \rightarrow 4OH^- \quad (8)$$

$$2Fe^{2+}(aq) + O_2(g) + 2H_2O \rightarrow 2FeOOH + 2H^+ \quad (9)$$

Equations (8) and (9) show that the formation of rust and corrosion of steel require sufficient H_2O and O_2. If any of the above reactions are prevented, corrosion is inhibited. Therefore, it was believed that by increasing the length of diffusion pathways via a suitable coating structure, this would effectively prevent H_2O and O_2 from contacting the substrate surface and thereby provide good anti-corrosion performance.

A schematic of the anti-corrosion mechanism of nanocomposite coatings on a metal surface was exhibited in Figure 15. The anti-corrosion mechanism was modelled by the morphology of the surface and cross section of the composite coating. As depicted in Figure 15a and d, the Zn-EP coating had the weakest corrosion resistance due to its loose surface structure and large gap between particles and particles, which makes corrosive media easily pass through the coating to reach the steel matrix. However, the corrosion protection of the EP coating increased markedly upon addition of 0.5 wt% GO or SiO_2–GO nanosheets. As depicted in Figure 15b and e, the GO nanosheets were well embedded in the Zn-EP coating to form a two-dimensional network structure. But, because of the poor dispersion of GO in the coating, there may be a phenomenon of agglomeration. As depicted in Figure 15c and f, compared with the GO/Zn-EP coating, the SiO_2–GO/Zn-EP coating had the superior corrosion inhibitive effect. The main reasons for this phenomenon are as follows: (1) SiO_2–GO nanoflakes could be dispersed more evenly in the Zn-EP substrate compared with GO, which could increase the barrier performance and cross-linking density of the epoxy resin, lengthening the diffusion channel of penetrant species in the coating substrate; (2) SiO_2–GO nanosheets greatly increased the contact angle with water, indicating the decreased hydrophilicity of the coating compared with GO filler and resulting in decreased water absorption by the SiO_2–GO nanocomposite coating; (3) SiO_2–GO nanosheets improve the coating adhesion on metallic substrate, leading to improve the barrier properties.

In conclusion, the addition of SiO_2–GO nanoflakes in Zn-EP coating greatly enhanced the hydrophobicity of the

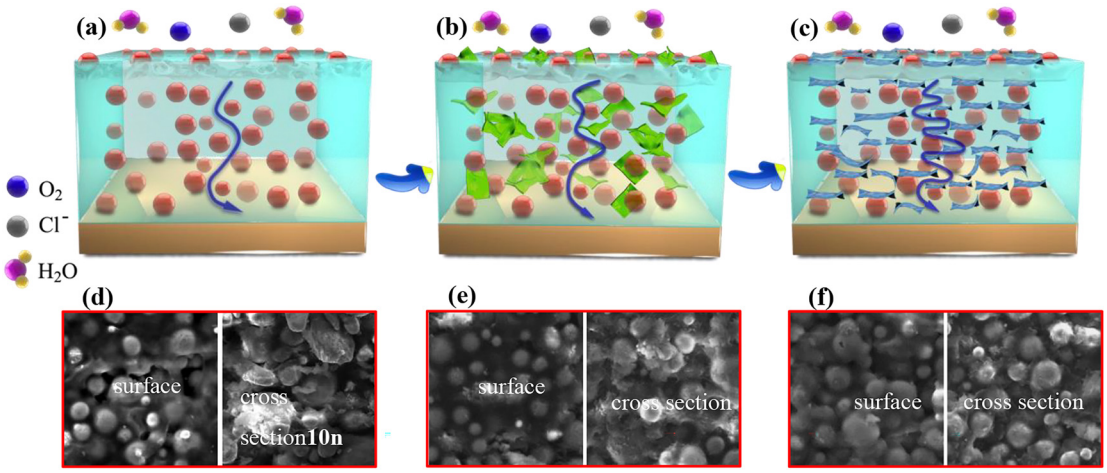

Figure 15: Schematic of the corrosion prevention mechanism of the nanocomposite coatings on the metal surface.
(a) Zn-EP coating; (b) GO/Zn-EP coating; (c) SiO_2–GO/Zn-EP coating; (d–f) were the surface morphology and the cross section morphology of the Zn-EP, GO/Zn-EP and SiO_2–GO/Zn-EP coatings, respectively.

coating surface, lengthened the transmission paths of corrosive ions to the substrate, and therefore improved the barrier properties and anticorrosive performance of the coating.

4 Conclusion

In summary, prepared SiO_2–GO nanosheets have an excellent anticorrosion properties when it as a filler for corrosion protection in a polymer matrix. The SiO_2–GO fillers could efficiently decrease the number of holes on the coating surface and to increase the barrier performance, this could be demonstrated by the CA increased from 56.8° to 85.1°. Also, the EIS test results show that the incorporation of 0.5 wt% SiO_2–GO in the Zn-EP coating improved the corrosion protection efficiency from 67.01 to 99.58%. These results showed that SiO_2–GO could enhance the adhesion between the sample and the metal matrix and enhanced the anticorrosion capacity of the coating surface through enhancing its barrier performance. Furthermore, once the coating was damaged by a scratch, the SiO_2–GO nanosheets also acted as a protective layer to cut off the electron transfer channel for galvanic corrosion, effectively inhibiting corrosion of the steel substrate.

Author contribution: All the authors have accepted responsibility for the entire content of this submitted manuscript and approved submission.
Research funding: We acknowledge financial support from the Scientific Research Fund of Shanxi Provincial Education Department (No. 19JK0861), the Industrial Innovation China of Key Research and Development Project of Shaanxi Province (No. 2019ZDLGY16-09) and the National Natural Science Foundation of China (No. 51672213).
Conflict of interest statement: The authors declare no conflicts of interest regarding this article.

References

Akbarinezhad, E., Ebrahimi, M., Sharif, F., Attar, M.M., and Faridi, H.R. (2011). Synthesis and evaluating corrosion protection effects of emeraldine base PAni/clay nanocomposite as a barrier pigment in zinc-rich ethyl silicate primer. Prog. Org. Coating 70: 39–44.

Alam, M.A., Sherif, E.S.M., and Al-Zahrani, S.M. (2013). Fabrication of various epoxy coatings for offshore applications and evaluating their mechanical properties and corrosion behavior. Int. J. Electrochem. Sci. 8: 3121–3131.

Ammar, S., Ramesh, K., Vengadaesvaran, B., Ramesh, S., and Arof, A.K. (2016). Amelioration of anticorrosion and hydrophobic properties of epoxy/PDMS composite coatings containing nano ZnO particles. Prog. Org. Coat. 92: 54–65.

Arman, S.Y., Ramezanzadeh, B., Farghadani, S., Mehdipour, M., and Rajabi, A. (2013). Application of the electrochemical noise to investigate the corrosion resistance of an epoxy zinc-rich coating loaded with lamellar aluminum and micaceous iron oxide particles. Corros. Sci. 77: 118–127.

Bahlakeh, G., Ramezanzadeh, B., and Ramezanzadeh, M. (2017). Cerium oxide nanoparticles influences on the binding and corrosion protection characteristics of a melamine-cured polyester resin on mild steel: an experimental, density functional theory and molecular dynamics simulation study. Corros. Sci. 118: 69–83.

Becerril, H.A., Mao, J., Liu, Z., Stoltenberg, R.M., Bao, Z., and Chen, Y. (2008). Evaluation of solution-processed reduced graphene oxide films as transparent conductors. ACS Nano 2: 463–470.

Bohm, S. (2014). Graphene against corrosion. Nat. Nanotechnol. 9: 741–742.

Chang, C.H., Huang, T.C., Peng, C.W., Yeh, T.C., Lu, H.I., Hung, W.I., Weng, C.J., Yang, T.I., and Yeh, J.M. (2012). Novel anticorrosion coatings prepared from polyaniline/graphene composites. Carbon 50: 5044–5051.

Chang, K.C., Ji, W.F., Lai, M.C., Hsiao, Y.R., Hsu, C.H., Chuang, T.L., Wei, Y., Yeh, J.M., and Liu, W.R. (2014). Correction: synergistic effects of hydrophobicity and gas barrier properties on the anticorrosion property of PMMA nanocomposite coatings embedded with graphene nanosheets. Polym. Chem. 5: 6865.

Chavrier, P., Lemaire, P., Revelant, O., Bravo, R., and Charnay, P. (1988). Characterization of a mouse multigene family that encodes zinc finger structures. Mol. Cell Biol. 8: 1319.

Cui, C., Lim, A.T.O., and Huang, J. (2017). A cautionary note on graphene anti-corrosion coatings. Nat. Nanotechnol. 12: 834–835.

Dashtizadeh, A., Abdouss, M., Mahdavi, H., and Khorassani, M. (2011). Acrylic coatings exhibiting improved hardness, solvent resistance and glossiness by using silica nano-composites. Appl. Surf. Sci. 257: 2118–2125.

Dhawade, P. and Jagtap, R. (2012). Comparative study of physical and thermal properties of chitosan-silica hybrid coatings prepared by sol–gel method. Chem. Sin. 3: 589–601.

Dhoke, S.K., Rajgopalan, N., and Khanna, A. (2013). Effect of nanoalumina on the electrochemical and mechanical properties of waterborne polyurethane composite coatings. J. Nanopart. 2013: 11.

Dong, R. and Liu, L.L. (2016). Preparation and properties of acrylic resin coating modified by functional graphene oxide. Appl. Surf. Sci. 368: 378–387.

Dreyer, D.R., Park, S., Bielawski, C.W., and Ruoff, R.S. (2010). The chemistry of graphene oxide. Chem. Soc. Rev. 39: 228–240.

Eduok, U., Jossou, E., and Szpunar, J. (2017). Enhanced surface protective performance of chitosanic hydrogel via nano-CeO_2 dispersion for API 5L X70 alloy: experimental and theoretical investigations of the role of CeO_2. J. Mol. Liq. 241: 684–693.

Gao, S.L., Mäder, E., and Plonka, R. (2008). Nanocomposite coatings for healing surface defects of glass fibers and improving interfacial adhesion. Compos. Sci. Technol. 68: 2892–2901.

Gergely, A., Pfeifer, E., Bertoti, I., Torok, T., and Kalman, E. (2011). Corrosion protection of cold-rolled steel by zinc-rich epoxy paint coatings loaded with nano-size alumina supported polypyrrole. Corros. Sci. 53: 3486–3499.

Hassan, H.H. (2007). Inhibition of mild steel corrosion in hydrochloric acid solution by triazole derivatives: part II: time and temperature effects and thermodynamic treatments. Electrochim. Acta 53: 1722–1730.

Ito, Y., Nyce, M., Plivelich, R., Klein, M., Steingart, D., and Banerjee, S (2011). Zinc morphology in zinc–nickel flow assisted batteries and impact on performance. J. Power Sources 196: 2340–2345.

Jalili, M., Rostami, M., and Ramezanzadeh, B. (2015). An investigation of the electrochemical action of the epoxy zinc-rich coatings containing surface modified aluminum nanoparticle. Appl. Surf. Sci. 328: 95–108.

Jiang, M.Y., Wu, L.K., Hu, J.M., and Zhang, J.Q. (2015a). Silane-incorporated epoxy coatings on aluminum alloy (AA2024). Part 1: improved corrosion performance. Corros. Sci. 92: 118–126.

Jiang, M.Y., Wu, L.K., Hu, J.M., and Zhang, J.Q. (2015b). Silane-incorporated epoxy coatings on aluminum alloy (AA2024). Part 2: mechanistic investigations. Corros. Sci. 92: 127–135.

Kalendova, A., Vesely, D., Kohl, M., and Stejskal, J. (2015). Anticorrosion efficiency of zinc-filled epoxy coatings containing conducting polymers and pigments. Prog. Org. Coat. 78: 1–20.

Kathi, J., and Rhee, K.Y. (2008). Surface modification of multi-walled carbon nanotubes using 3-aminopropyltriethoxysilane. J. Mater. Sci. 43: 33–37.

Kim, J., Cote, L.J., Kim, F., Yuan, W., Shull, K.R., and Huang, J. (2010). Graphene oxide sheets at interfaces. J. Am. Chem. Soc. 132: 8180–8186.

Konios, D., Stylianakis, M.M., Stratakis, E., and Kymakis, E. (2014). Dispersion behaviour of graphene oxide and reduced graphene oxide. J. Colloid Interface Sci. 430: 108–112.

Layek, R.K. and Nandi, A.K. (2013). A review on synthesis and properties of polymer functionalized graphene. Polymer 54: 5087–5103.

Liu, X.W., Xiong, J.P., Lv, Y.W., and Zuo, Y. (2009). Study on corrosion electrochemical behavior of several different coating systems by EIS. Prog. Org. Coat. 64: 497–503.

Liu, Y., Liu, J.Y., Deng, C.H., and Zhang, X.M. (2011). Graphene and graphene oxide: two ideal choices for the enrichment and ionization of long-chain fatty acids free from matrix-assisted laser desorption/ionization matrix interference. Rapid Commun. Mass Spectrom. 25: 3223–3234.

Liu, Y., Meng, X.G., Liu, Z.C., Meng, M.J., Jiang, F.P., Luo, M., Ni, L., Qiu, J., Liu, F.F., and Zhong, G.X. (2015). Preparation of a two-dimensional Ion-Imprinted polymer based on a graphene oxide/SiO_2 composite for the selective adsorption of nickel ions. Langmuir 31: 8841–8851.

Lu, H., Zhang, S.T., Li, W.H., Cui, Y.N., and Yang, T. (2017). Synthesis of graphene oxide-based sulphonated Oligoanilines coatings for synergistically enhanced corrosion protection in 3.5% NaCl solution. ACS Appl. Mater. Interfaces 9: 4034–4043.

Mahulikar, P.P., Jadhav, R.S., and Hundiwale, D.G. (2011). Performance of polyaniline/TiO_2 nanocomposites in epoxy for corrosion resistant coatings. Iran. Polym. J. (Engl. Ed.) 20: 367–376.

Maksimovic, M.D., and Miskovic-Stankovic, V.B. (1992). The corrosion behaviour of epoxy-resin electrocoated steel. Corrosion Sci. 33: 271–279.

Mirabedini, S., Behzadnasab, M., and Kabiri, K. (2012). Performance of polyaniline/TiO_2 nanocomposites in epoxy for corrosion resistant coatings. Compos. Part. A. Appl. Sci. Manuf. 43: 2095–2106.

Mo, M.T., Zhao, W.J., Chen, Z.F., Yu, Q.X., Zeng, Z.D., Wu, X.J., and Xue, Q. (2015). Excellent tribological and anti-corrosion performance of polyurethane composite coatings reinforced with functionalized graphene and graphene oxide nanosheets. RSC Adv. 5: 56486–56497.

Najjar, R., Katourani, S.A., and Hosseini, M.G. (2018). Self-healing and corrosion protection performance of organic polysulfide@urea-formaldehyde resin core-shell nanoparticles in epoxy/PANI/ZnO nanocomposite coatings on anodized aluminum alloy. Prog. Org. Coating 124: 110–121.

Pourhashem, S., Vaezi, M.R., and Rashidi, A. (2017). Investigating the effect of SiO_2-graphene oxide hybrid as inorganic nanofiller on corrosion protection properties of epoxy coatings. Surf. Coating. Technol. 311: 282–294.

Ozyılmaz, A.T., Erbil, M., and Yazici, B. (2006). The corrosion behaviours of polyaniline coated stainless steel in acidic solutions. Thin Solid Films 496: 431–437.

Parhizkar, N., Ramezanzadeh, B., and Shahrabi, T. (2018). The epoxy coating interfacial adhesion and corrosion protection properties enhancement through deposition of cerium oxide nanofilm modified by graphene oxide. J. Ind. Eng. Chem. 744: 728–739.

Ramezanzadeh, B., Ghasemi, E., Askari, F., and Mahdavian, M. (2015). Synthesis and characterization of a new generation of inhibitive pigment based on zinc acetate/benzotriazole: solution phase and coating phase studies. Dyes Pigm. 122: 331–345.

Ramezanzadeh, B., Ahmadi, A., and Mahdavian, M. (2016a). Enhancement of the corrosion protection performance and cathodic delamination resistance of epoxy coating through treatment of steel substrate by a novel nanometric sol-gel based silane composite film filled with functionalized graphene oxide nanosheets. Corros. Sci. 109: 182–205.

Ramezanzadeh, B., Haeri, Z., and Ramezanzadeh, M. (2016b). A facile route of making silica nanoparticles-covered graphene oxide nanohybrids (SiO_2-GO); fabrication of SiO_2-GO/epoxy composite coating with superior barrier and corrosion protection performance. Chem. Eng. J. 303: 511–528.

Ramezanzadeh, B., Niroumandrad, S., Ahmadi, A., Mahdavian, M., and Moghadam, M.H.M. (2016c). Enhancement of barrier and corrosion protection performance of an epoxy coating through wet transfer of amino functionalized graphene oxide. Corros. Sci. 103: 283–304.

Ramezanzadeh, B., Moghadam, M.H.M., Shohani, N., and Mahdavian, M (2017). Effects of highly cystalline and conductive polyaniline/graphene oxide composites on the corrosion protection performance of a zinc-rich epoxy coating. Chem. Eng. J. 320: 363–375.

Remyamol, T., John, H., and Gopinath, P. (2013). Synthesis and nonlinear optical properties of reduced graphene oxide covalently functionalized with polyaniline. Carbon 59: 308–314.

Stejskal, J., Trchova, M., Brodinova, J., Kalenda, P., Fedorova, S.V., Prokes, J., and Zemek, J. (2006). Coating of zinc ferrite particles with a conducting polymer, polyaniline. J. Colloid Interface Sci. 298: 87–93.

Schaefer, K. and Miszczyk, A. (2013). Improvement of electrochemical action of zinc-rich paints by addition of nanoparticulate zinc. Corros. Sci. 66: 380–391.

Shi, G., Zhang, M.Q., Rong, M.Z., Wetzel, B., and Friedrich, K. (2003). Friction and wear of low nanometer Si_3N_4 filled epoxy composites. Wear 254: 784–796.

Shi, S.E., Zhang, Z.M., and Yu, L.M. (2017). Hydrophobic polyaniline/modified SiO_2 coatings for anticorrosion protection. Synth. Met. 233: 94–100.

Shi, X.M., Nguyen, T.A., Suo, Z.Y., Liu, Y.J., and Avci, R. (2009). Effect of nanoparticles on the anticorrosion and mechanical properties of epoxy coating. Surf. Coat. Technol. 204: 237–245.

Sharif, F., and Gudarzi, M.M. (2012). Enhancement of dispersion and bonding of graphene-polymer through wet transfer of functionalized graphene oxide. Express Polym. Lett. 6: 1017–1031.

Syed, J.A., Tang, S.C., and Meng, X.K. (2017). Super-hydrophobic multilayer coatings with layer number tuned swapping in surface wettability and redox catalytic anti-corrosion application. Sci. Rep. 7: 4403.

Treossi, E., Melucci, M., Liscio, A., Gazzano, M., Samori, P., and Palermo, V. (2009). High-contrast Visualization of graphene oxide on Dye-sensitized glass, Quartz, and silicon by Fluorescence Quenching. J. Am. Chem. Soc. 131: 15576.

Wang, X., Xing, W.Y., Song, L., Yu, B., Hu, Y., and Yeoh, G.H. (2013). Preparation of UV-curable functionalized graphene/polyurethane acrylate nanocomposite with enhanced thermal and mechanical behaviors. React. Funct. Polym. 73: 854–858.

Wan, Y.J., Gong, L.X., Tang, L.C., Wu, L.B., and Jiang, J.X. (2014). Mechanical properties of epoxy composites filled with silane-functionalized graphene oxide. Compos. Part A Appl. Sci. Manuf. 64: 79–89.

Yang, X.Y., Wang, X.B., Yang, J., Li, J., and Wan, L. (2013). Functionalization of graphene using trimethoxysilanes and its reinforcement on polypropylene nanocomposites. Chem. Phys. Lett. 570: 125–131.

Yang, H.F., Li, F.H., Shan, C.S., Han, D.X., Zhang, Q.X., Niu, L., and Ivaska, A. (2009). Covalent functionalization of chemically converted graphene sheets via silane and its reinforcement. J. Mater. Chem. 19: 4632–4638.

Yu, Z.X., Di, H.H., Ma, Y., He, Y., Liang, L., Lv, L, Ran, X., Pan, Y., and Luo, Z. (2015). Preparation of graphene oxide modified by titanium dioxide to enhance the anti-corrosion performance of epoxy coatings. Surf. Coating. Technol. 276: 471–478.

Zaslavsky, B.Y., Gulaeva, N.D., Djafarov, S., Masimov, E.A., and Miheeva, L.M. (1990). Phase separation in aqueous poly(ethylene glycol)-$(NH_4)_2SO_4$ systems and some physicochemical properties of the phases. J. Colloid Interface Sci. 137: 147–156.

Zhang, W.L. and Choi, H.J. (2012). Silica-graphene oxide hybrid composite particles and their electroresponsive characteristics. Langmuir 28: 7055–7062.

Zhang, X.Z., Wang, F.H., and Du, Y.L. (2007). Effect of nano-sized titanium powder addition on corrosion performance of epoxy coatings. Surf. Coat. Technol. 201: 7241–7245.

Zhu, C.Z., Han, L., Hu, P., and Dong, S.J. (2012). In situ loading of well-dispersed gold nanoparticles on two-dimensional graphene oxide/SiO_2 composite nanosheets and their catalytic properties. Nanoscale 4: 1641–1646.